electronics

MDPI

Article

Reactive Shield for Reducing the Magnetic Field of a Wireless Power Transfer System with Dipole Coil Structure

Yujun Shin [1] and Seongho Woo [2,*]

[1] Automotive Engineering, Department of Smart Mobility Engineering, Keimyung University, Daegu 42601, Republic of Korea; yjshin@kmu.ac.kr
[2] Cho Chun Shik Graduate School of Mobility, Korea Advanced Institute of Science and Technology, Daejeon 34051, Republic of Korea
* Correspondence: seongho@kaist.ac.kr

Abstract: This paper proposes a reactive shield structure to reduce the leakage magnetic field of a wireless power transfer (WPT) system with a dipole coil structure. The reactive shield resonates at a frequency lower than that of the WPT system and operates in an inductive region where the reactance is positive. Therefore, the magnetic field generated by the shield coil is 180° different in phase from that generated by the transmitting coil, resulting in an effective reduction in the leakage magnetic field. The methodology for designing the reactive shield for the dipole coil structure is mathematically analyzed, and the current and magnetic field phases are compared. Its effectiveness has been validated through simulations and experiments. Specifically, the proposed method is validated through a 50 W class WPT experiment, which showed that the proposed shielding structure achieves efficiency reductions ranging from 0.3% to 1.5% and has a leakage magnetic field reduction effect of up to 67% compared to the comparison groups.

Keywords: wireless power transfer; reactive shield; dipole coils; mutual inductance; magnetic field

Citation: Shin, Y.; Woo, S. Reactive Shield for Reducing the Magnetic Field of a Wireless Power Transfer System with Dipole Coil Structure. *Electronics* **2024**, *13*, 1712. https://doi.org/10.3390/electronics13091712

Academic Editor: Enzo Pasquale Scilingo

Received: 6 April 2024
Revised: 24 April 2024
Accepted: 27 April 2024
Published: 29 April 2024

1. Introduction

Wireless power transfer (WPT) technology has garnered significant attention as a viable replacement for wired power transfer [1–3]. WPT systems transfer energy through a magnetic field without connecting a conductor between the transmitting side (TX) and the receiving side (RX). Therefore, the WPT system is safe, eliminating the risk of electric shock, and convenient as it does not require a separate physical connection [4,5]. In particular, as various applications operate using electrical energy and batteries are essential, the WPT system is receiving significant attention as a battery charging technology [6]. Representative examples of WPT system applications are being studied in various areas, including electric vehicles, mobile applications, industrial electronics, and biomedical devices [7–9].

The most commonly used coil structure in WPT systems is the planar-type coil, as shown in Figure 1 [10,11]. As shown in Figure 1a, WPT systems with planar-type coils face each other. This is because the magnetic field is transmitted from the TX side to the RX side in a direction perpendicular to the coil, as shown in Figure 1b. Consequently, the wider the cross-sectional area of the coil, the better the various characteristics of the WPT system, including power transfer efficiency and power transfer capacity [12–14].

However, securing a large coil cross-sectional area is not feasible in certain applications. For example, in biomedical device applications where WPT systems are widely used, securing a large coil cross-sectional area is challenging [9,15,16]. Additionally, in-home appliance applications, such as wireless charging between monitors or televisions, the cross-sectional area where TX and RX face each other is often very narrow [17].

In applications with such a narrow coil cross-sectional area, a dipole-type coil is used instead of a planar-type coil [18–21]. The dipole coil shape is shown in Figure 2. The dipole-type coil has a structure in which the coil is wound around a magnetic material

(ferrite) with high magnetic permeability, such as a solenoid. Figure 2b shows how the magnetic field is transmitted from TX to RX in the dipole-type coil. It can be observed that most of the magnetic field in the dipole-type coil is transmitted through the magnetic core, and the magnetic field is transmitted from the TX to RX coils at both ends of the magnetic core. The amount of magnetic field transmitted is significantly less dependent on the area facing the WPT coil system than on the planar type. Therefore, the dipole coil structure is used in various applications where the area facing each other is very narrow.

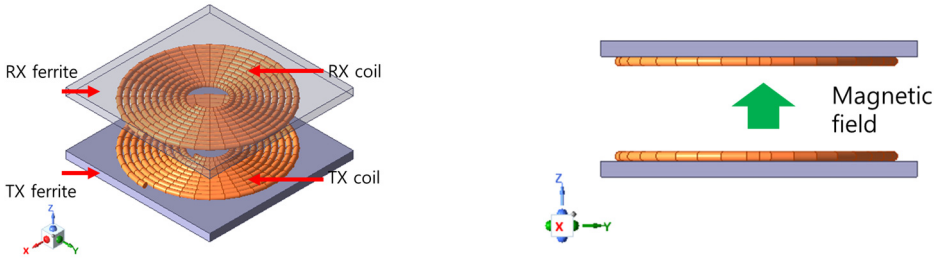

Figure 1. Structure of typical planar WPT coils: (**a**) bird's-eye view and (**b**) the shape of the magnetic field.

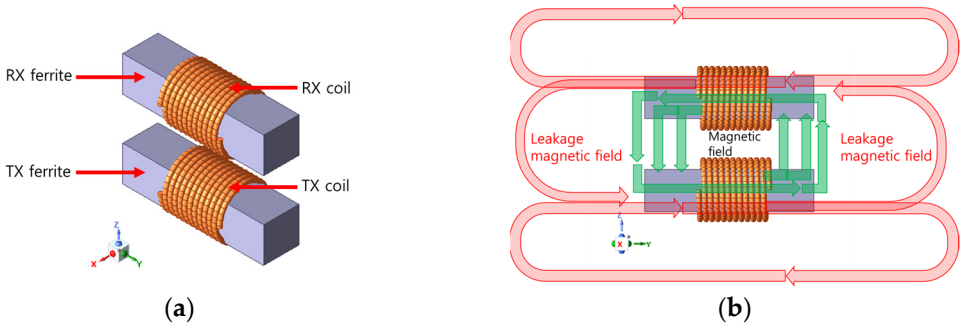

Figure 2. Structure of dipole-type WPT coils: (**a**) bird's-eye view and (**b**) the shape of the magnetic field.

However, the dipole coil structure has a major disadvantage compared to the planar-type coil structure, which is the problem of leakage magnetic fields [18]. In a planar-type coil, the magnetic field is mainly transmitted between the magnetic cores, whereas in the dipole coil structure, it radiates outward from the ends of the magnetic core, as shown in Figure 2b. Due to the nature of the dipole structure in which the magnetic field radiates in the longitudinal direction, it is very difficult to reduce leakage magnetic fields. This drawback of the dipole coil structure poses a significant obstacle to its application in devices that are inevitably sensitive to leakage magnetic fields. For example, devices used near the human body must meet the ICNIRP 1998 standard for magnetic field strength [18], and biomedical devices used very closely to the human body must meet the Specific Absorption Rate (SAR) standard [19].

Research on WPT systems with dipole structures has been extensive [20–24]. First, Choi et al. [20] and Park et al. [21] proposed a method for transmitting power over a relatively long distance using a dipole structure. Specifically, they found that the effectiveness of the dipole coil structure was maximized when the cross-sectional area between the TX and RX sections was small compared to the power transfer distance. In addition, Rong et al. [22] proposed a WPT system capable of transferring power omnidirectionally in low-power applications using multiple dipole coils, and Rong et al. [23] studied an angle-free WPT system with a similar structure. Moreover, in Khan et al.'s study [24], the WPT system was applied using a dipole coil structure in a missile application with a small cross-sectional area where the TX and RX sections faced each other. However, in the above-mentioned WPT systems using the dipole structure, no mention was made of

reducing the leakage magnetic field of the corresponding structure. In fact, there has been no research to date on reducing the leakage magnetic field of the dipole structure.

Among the methods for reducing magnetic leakage from planar coils, the most actively researched is the reactive shield (SH) method [25–27]. Park et al. [25] proposed a method to reduce magnetic leakage in a WPT system using a planar coil for mobile applications. In Kim et al.'s study [27], power transfer efficiency was increased, and the leakage magnetic field was reduced using a dual-loop reactive shield. Furthermore, Wei and Wu [28] studied similar content using the frequency split phenomenon. However, these reactive shield methods all have the limitation that they apply only to planar coils. The reason why so much research has only been conducted on magnetic field reduction methods in planar-type WPT coils is because, as can be seen in Figure 1b, the magnetic field radiating outward from this type of coil is relatively smaller than that of the dipole type.

This paper proposes a reactive shield coil structure to minimize leakage magnetic fields from a WPT system with a dipole-type coil. The proposed reactive shield generates an induced voltage by Faraday's law. The induced voltage generates a current with an opposite phase to the magnetic field generated from the WPT coil, thereby producing a magnetic field with an opposite phase. Therefore, the magnetic fields are canceled at both ends of the magnetic material, reducing the leakage magnetic field. Section 2 provides a mathematical analysis of the reactive shield for the dipole structure. Section 3 confirms the shield performance through simulation, while Section 4 validates the performance of the proposed shield structure through experimentation. Finally, Section 5 presents the conclusion of this paper.

2. Principle of Reactive Shield for Dipole Coil Type

The dipole-type WPT coil with the proposed reactive shield applied is shown in Figure 3. The proposed reactive shield has a structure in which reactive shield coils are added to both sides of the TX coil in a typical dipole-type coil, as shown in Figure 2. The RX side lacks a separate reactive shield structure because WPT systems with a dipole coil structure are generally designed in very narrow spaces, especially considering the severe spatial constraints of the RX. Therefore, only the TX side, with fewer spatial constraints, has a re-active shield structure. As will be validated in Sections 3 and 4, the leakage magnetic field from the coil of the dipole structure can be reduced, even with a shield structure only on the TX side.

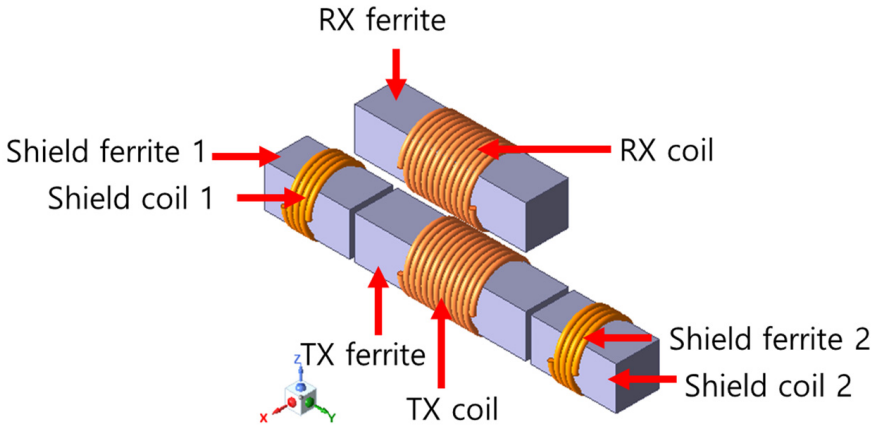

Figure 3. Dipole-type WPT coil with the proposed reactive shield.

The equivalent circuit of the dipole-type WPT system with the proposed shield structure in Figure 3 is shown in Figure 4. Figure 4a shows the entire circuit from direct current (DC) input to DC output. The input DC voltage (Vin) is converted into an alternating current (AC) component through an inverter and transferred as a DC voltage (V_{load}) to the load (R_{load}) through resonant circuits, coils, and a rectifier. The resonant circuit for impedance compensation adopted the LCC-series topology, known for its constant voltage

out-put characteristics, and its effectiveness has been proven in various studies [12,28–31]. In addition, as the resonant circuit on the RX side only has a capacitor, it provides spatial advantages on the RX side and is suitable for a dipole-structured coil. As shown in Figure 3, there are four coils (TX, RX, SH1, and SH2), resulting in six types of mutual inductance between coils, as shown in Figure 4a (four combinations of two).

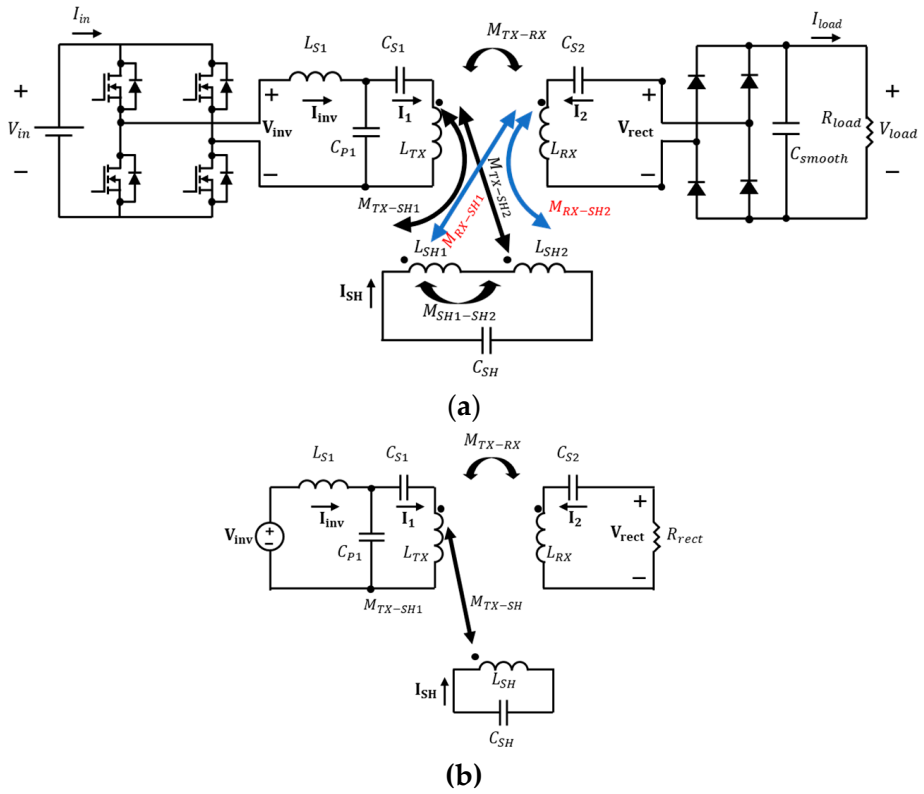

Figure 4. WPT equivalent circuit with proposed reactive shield structure: (**a**) actual circuit diagram and (**b**) simplified equivalent circuit considering only AC components.

Figure 4b is a simplified and approximated circuit of Figure 4a. In Figure 4b, $\mathbf{V_{inv}}$ represents the root mean square (RMS) value of the fundamental component of the inverter output voltage. This has a relationship (1) with the V_{in}:

$$\mathbf{V_{inv}} = \frac{4}{\pi\sqrt{2}} V_{in} \angle 0^{\circ} \tag{1}$$

As $\mathbf{V_{inv}}$ is an RMS value, all voltages and currents in Figure 4a,b are RMS values. Additionally, the load resistance (R_{rect}) seen from the rectifier is as shown in (2):

$$R_{rect} = \frac{8}{\pi^2} R_{load} \tag{2}$$

Furthermore, the six magnetic couplings (mutual inductances) approximate only two meaningful mutual inductances. First, the mutual inductance between the TX and RX coils ($M_{TX\text{-}RX}$) is significant in the WPT system. Second, because RX and shield coils (SH1 and SH2) are sufficiently far apart magnetically, the corresponding mutual inductances ($M_{RX\text{-}SH1}$, $M_{RX\text{-}SH2}$) are ignored:

$$M_{RX\text{-}SH1} = M_{RX\text{-}SH2} \simeq 0 \tag{3}$$

Third, the resonant capacitor of the shield coils is selected simultaneously by winding the two shield coils in series. Specifically, the two shield coils are viewed as one. Therefore, the relationships between L_{SH1} and L_{SH2} in Figure 4a and L_{SH} in Figure 4b are as follows (4):

$$L_{SH} = L_{SH1} + L_{SH2} + 2M_{SH1\text{-}SH2} \simeq L_{SH1} + L_{SH2} \tag{4}$$

As shown in Figure 3, the SH coils are sufficiently far apart, making the mutual inductance ($M_{SH1\text{-}SH2}$) between them negligible. Finally, because L_{SH1} and L_{SH2} are connected in series, the relationships between $M_{TX\text{-}SH1}$ and $M_{TX\text{-}SH2}$ in Figure 4a and $M_{TX\text{-}SH}$ in Figure 4b can be expressed as follows (5):

$$M_{TX\text{-}SH} = M_{TX\text{-}SH1} + M_{TX\text{-}SH2} \tag{5}$$

All approximations will be validated through simulation in Appendix A.

Next, the resonant condition on the TX side follows that of the LCC topology [12]. This is equivalent to (6), and the resulting TX coil current ($\mathbf{I_1}$) is equivalent to (7):

$$\frac{1}{\sqrt{L_{S1}C_{P1}}} = \frac{1}{\sqrt{(L_{TX} - L_{S1})C_{S1}}} = \omega_{n1} = \omega_o \tag{6}$$

$$\mathbf{I}_1 = -j\omega_o C_{P1}\mathbf{V_{inv}} = -j\frac{4}{\pi\sqrt{2}}\omega_o C_{P1} V_{in}\angle 0^\circ \tag{7}$$

In (6), ω_{n1} is the resonant frequency of the TX side, and ω_o is the operating frequency of the inverter. Additionally, the resonant condition of the RX side is a series topology, so it is equal to (8), and the voltage delivered to the load (R_{rect}) due to mutual inductance is equal to (9):

$$\frac{1}{\sqrt{L_{RX}C_{S2}}} = \omega_{n2} = \omega_o \tag{8}$$

$$\mathbf{V_{rect}} = j\omega_o M_{TX\text{-}RX}\mathbf{I}_1 = \omega_o^2 M_{TX\text{-}RX} C_{P1}\mathbf{V_{inv}} \tag{9}$$

In (8), ω_{n2} is the resonant frequency of the RX side.

Meanwhile, the resonant circuit on the SH side is adjusted with a capacitor (C_{SH}), as shown in Figure 4. Studies have found that for the magnetic field generated in the SH coil to have an opposite phase of the magnetic field generated in the TX coil, the resonant frequency of the SH coil (ω_{SH}) must be set lower than that of the system operating frequency (ω_o) [25–27]. In essence, the resonant of the SH coil must be in the inductive region, as shown in Figure 5a,b.

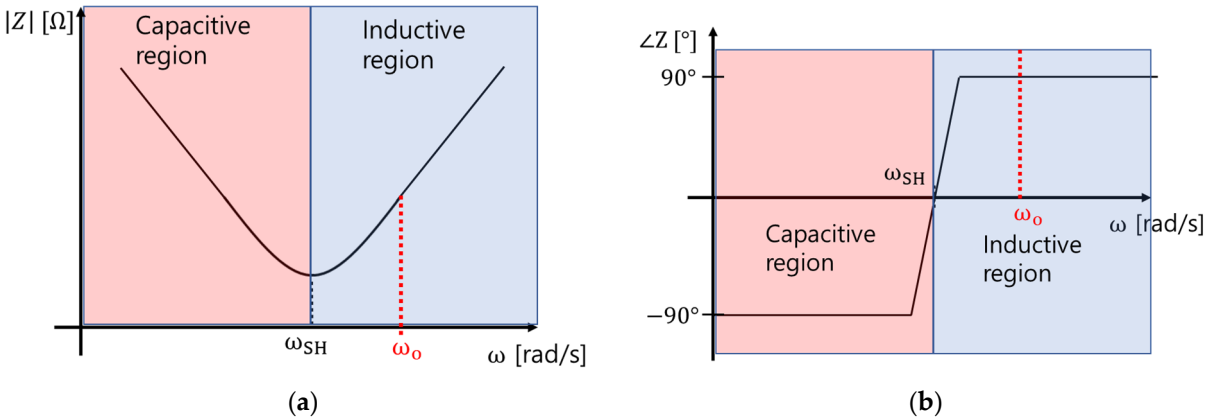

Figure 5. Impedance comprising the SH coil (L_{SH}) and resonant circuit (C_{SH}): (**a**) impedance magnitude and (**b**) impedance phase.

To have the above relationship, the impedance of the SH coil must be equal to (10) and (11):

$$Z_{SH} = j\left(\omega_o L_{SH} - \frac{1}{\omega_o C_{SH}}\right) = j\omega_o L_{eq} \tag{10}$$

$$\frac{1}{\sqrt{L_{SH}C_{SH}}} = \omega_{SH} < \omega_o \tag{11}$$

In (10), the resonant condition on the SH coil side is in the inductive region, so L_{eq} is the equivalent inductance. According to Faraday's law, voltage is induced in the SH coil by the TX coil current, as shown in (12), if the resonant condition on the SH side is equal to (10) and (11), and the current ($\mathbf{I_{SH}}$) flowing through the SH coil is equal to (13):

$$\mathbf{V_{SH}} = j\omega_o M_{TX\text{-}SH}\mathbf{I}_1 \tag{12}$$

$$\mathbf{I_{SH}} = \frac{-j\omega_o M_{TX\text{-}SH}\mathbf{I}_1}{Z_{SH}} = -\frac{M_{TX\text{-}SH}}{L_{eq}}\mathbf{I}_1 \tag{13}$$

As seen in (13), the current phase of the SH coil ($\mathbf{I_{SH}}$) is 180° different from that of the TX coil ($\mathbf{I_1}$).

In Figure 3, the dipole shares the same structure as the solenoid; hence, the magnetic field at its end equals (14):

$$B_{coil} \simeq \mu n I_{coil} \tag{14}$$

Therefore, the phase of the magnetic field generated in the coils aligns with the coil current. Specifically, as the currents in the TX and SH coils have a 180° phase difference, as shown in (13), the magnetic field generated in the TX coil will be reduced by that generated in the SH coil. Figure 6 shows a phasor diagram of the magnetic field of the WPT system with and without the SH coil. As shown in Figure 6a, without an SH coil, only the sum of the magnetic fields generated from the TX and RX coils exists. However, with an SH coil, the magnetic field ($\mathbf{B_{SH}}$) caused by the SH coil reduces the magnetic field of the TX coil ($\mathbf{B_{TX}}$), thereby reducing the vector sum ($\mathbf{B_{total}}$) of the magnetic field. Moreover, as can be seen in Figure 3, since the SH coil is wound in high permeability ferrite, the magnetic field generated by the SH ($\mathbf{B_{SH}}$) coil will become stronger and cancel out the magnetic field of the TX coil ($\mathbf{B_{TX}}$).

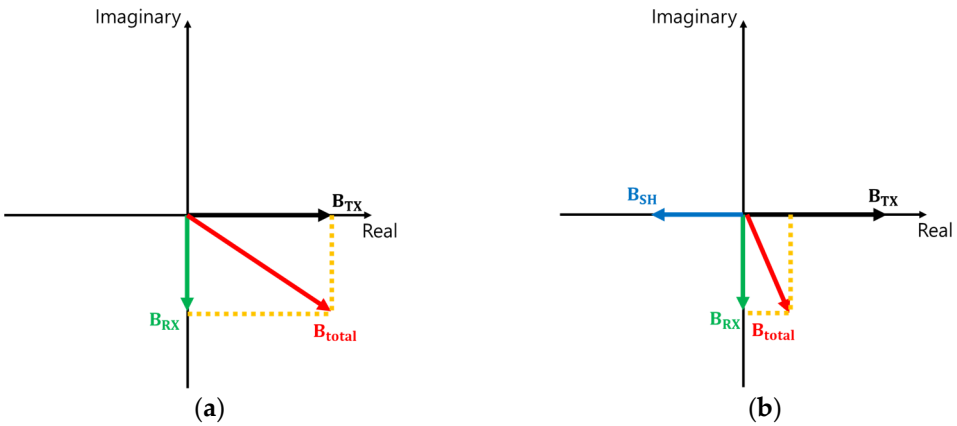

Figure 6. Vector sum of magnetic fields in the WPT coil: (**a**) vector sum when SH coil is not applied and (**b**) vector sum when SH coil is applied.

The magnetic fields of the TX and SH coils have opposite phases, causing them to cancel each other, as depicted in Figure 7. This figure shows only the TX, RX, and SH coils; the magnetic core (ferrite) is omitted to emphasize the magnetic field. For the standard of current and magnetic field phase, a dot convention is indicated for each coil. The TX and SH coil currents have a phase difference of 180°. Therefore, in the direction where

the magnetic field of the TX coil goes out, the counterpart SH coil (L_{SH2}) is also generated in the outgoing direction. Similarly, in the direction where the magnetic field of the TX coil enters the coil, a magnetic field is generated in the direction where the counterpart SH coil (L_{SH1}) also enters. However, the TX magnetic field, essential for power transfer, passes through without cancellation and reaches the RX coil. In essence, the reactive SH coil cancels unnecessary leakage magnetic fields, allowing only the magnetic fields essential for the WPT to reach the RX coil. The reactive shield for the dipole-type coil limits the magnetic field of the WPT coils and reduces the leakage magnetic field.

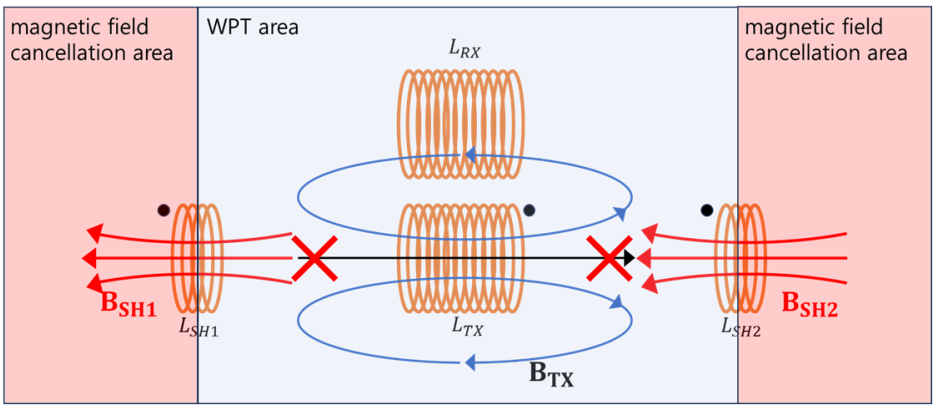

Figure 7. Magnetic field configuration according to the area in the reactive shield structure for the proposed dipole structure.

3. Validation of the Effectiveness of the Proposed Reactive Shield through Simulation

Figure 8a is WPT coils with the proposed reactive shield, as shown in Figure 3, and Figure 8b,c are comparison groups to validate the reactive shield performance. Figure 8c, unlike Figure 8a, has a structure in which only ferrite is added without SH coils. In other words, both Figure 8b,c are structures in which the reactive shield structure is not applied. The geometric information of each coil model is shown in Figure 8. In addition, Table 1 lists the remaining information on the simulation (operating frequencies, air gaps, and wire information). In Figure 8a–c, note that the color of the magnetic material on the SH side is shown in gray, and the color of the magnetic material on the WTP coil side is shown in blue. This is simply to distinguish the magnetic material structure and the permeability of all magnetic materials is the same. Table 2 summarizes the information on the coils extracted by performing magnetic field simulation with the setup in Figure 8 and Table 1. The notation for each inductance matches the circuit in Figure 4.

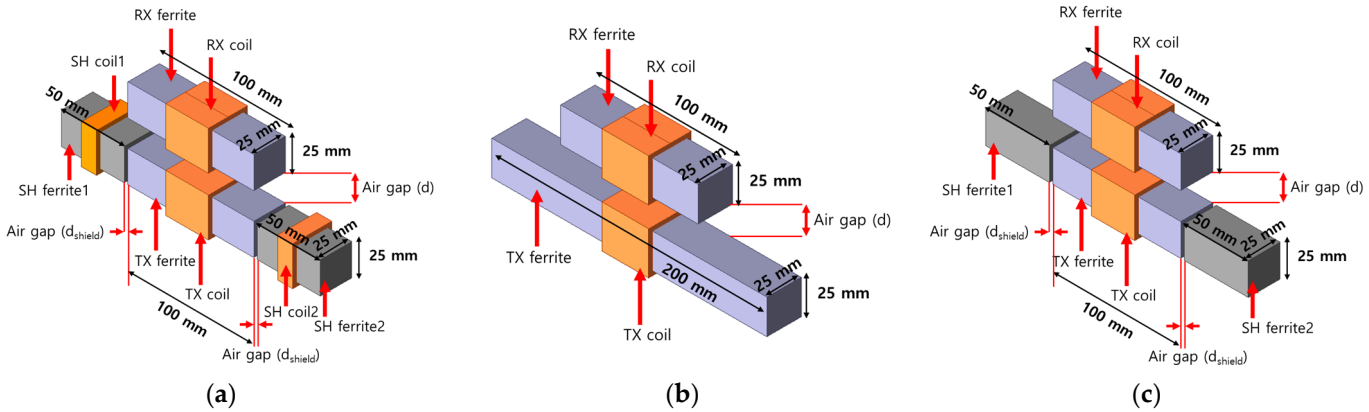

Figure 8. Simulation illustration of the proposed reactive shield structure and comparison groups: (**a**) proposed structure; (**b**) comparison Case 1—case with long TX ferrite; (**c**) comparison Case 2—case in which only SH ferrite is added.

Table 1. Additional information on magnetic field simulation.

Parameters	Value
Operating frequency	85 kHz
Relative permeability of magnetic core (TX, RX, SH)	150
Air gap (d)	15 mm
Air gap (d_{shield})	3 mm
Diameter of coil wire	2.8 mm
Number of turns of TX and RX coils	12 turns
Number of turns of SH coil	4 turns

Table 2. Inductance extraction results through magnetic field simulation.

Model	Parameters	Value [μH]
Proposed model	Inductance of TX coil (L_{TX})	29.52
	Inductance of RX coil (L_{RX})	25.41
	Mutual inductance between TX and RX ($M_{TX\text{-}RX}$)	6.2
	Inductance of SH coils (L_{SH1}, L_{SH2})	5.82
	Mutual inductance between SH and TX ($M_{TX\text{-}SH}$)	3.91
Comparison Case 1	Inductance of TX coil (L_{TX})	35.76
	Inductance of RX coil (L_{RX})	25.62
	Mutual inductance between TX and RX ($M_{TX\text{-}RX}$)	7.15
Comparison Case 2	Inductance of TX coil (L_{TX})	29.57
	Inductance of RX coil (L_{RX})	25.44
	Mutual inductance between TX and RX ($M_{TX\text{-}RX}$)	6.21

Table 3 shows the resonant circuit values for each case. Please refer to Figure 4 for the notation of resonant circuit values. In the circuit simulation, the V_{in} of Figure 4 is 60 V, and the target TX current ($\mathbf{I_1}$) is selected as 6 A_{RMS}. Based on the selected values, each resonant circuit value is calculated through (6) to (8). All resonant frequencies except for the SH coil are set to 85 kHz, matching the system operating frequency. Additionally, the SH frequency of the proposed model is selected as 50 kHz (f_{SH} = 50 kHz). The power delivered to the final load resistance (R_{load}) is 50 W in all three cases. The current magnitude of each part for 50 W of power to be delivered to the loads is summarized in Table 4. Due to the characteristics of the LCC topology, the TX coil currents are all identical, while the RX coil currents vary. Notably, the output current required to deliver 50 W to the load is the largest for the proposed model.

Table 3. Resonant circuit parameters for circuit simulation.

Model	Parameters	Value
Proposed model	TX series inductance (L_{S1})	16.8 μH
	TX parallel capacitance (C_{P1})	208 nF
	TX series capacitance (C_{S1})	302 nF
	RX series capacitance (C_{S2})	140 nF
	SH capacitance (C_{SH})	1740 nF
Comparison Case 1	TX series inductance (L_{S1})	16.8 μH
	TX parallel capacitance (C_{P1})	208 nF
	TX series capacitance (C_{S1})	217 nF
	RX series capacitance (C_{S2})	138 nF
Comparison Case 2	TX series inductance (L_{S1})	16.8 μH
	TX parallel capacitance (C_{P1})	208 nF
	TX series capacitance (C_{S1})	217 nF
	RX series capacitance (C_{S2})	139 nF

Table 4. Current in each coil when transmitting 50 W of power.

Model	Parameters	Value
Proposed model	Current of TX coil (I_1) Current of RX coil (I_2) Current of SH coil (I_{SH}) Phase difference between TX current and SH current	6 A_{RMS} 2.35 A_{RMS} 5.6 A_{RMS} 177°
Comparison Case 1	Current of TX coil (I_1) Current of RX coil (I_2)	6 A_{RMS} 1.98 A_{RMS}
Comparison Case 2	Current of TX coil (I_1) Current of RX coil (I_2)	6 A_{RMS} 2.21 A_{RMS}

Figure 9 shows the simulation setup for leakage magnetic field measurements. To simulate the leakage magnetic field measurement, the currents in Table 4 are applied to the dipole coil structures in Figure 8. The magnitude of the current and the phase difference between the currents are considered. In the *x*-axis direction, measurements are made starting from the center of the TX and RX coil air gap, while in the *y*-axis direction, measurements are made in the longitudinal direction from the end of the magnetic material. Additionally, in the z direction, the magnetic field is simulated upward from the end of the RX coil. Simulations are performed to measure the magnetic field from 0 to 300 mm in all axial directions. Moreover, the magnetic field simulation method shown in Figure 9 is performed identically for all coils in Figure 8.

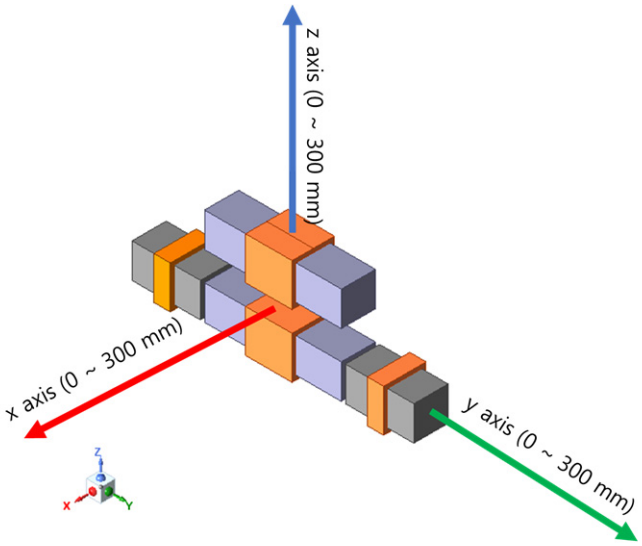

Figure 9. Magnetic field measurement for leakage magnetic field simulation.

Figure 10 shows the magnetic field simulation results. In Figure 10a–c, the proposed case shown in the blue line is the case to which the shield structure is applied, and comparison Case 1 on the orange line and comparison Case 2 on the yellow line are both cases where the shield is not applied. As shown in Figure 10a–c, the magnetic field is the lowest in the dipole coil structure with the proposed reactive shield in all directions. The case with the next lowest magnetic field level is comparison Case 2 in Figure 8c, attributed to the addition of ferrites on both sides of the TX coil, which partially inhibits the magnetic field from leaking outside. Finally, in comparison Case 1 in Figure 8b, the TX magnetic core has a long ferrite bar, and in this case, the leakage magnetic field is the highest. Moreover, a common belief suggests that in a planar coil, large or thick magnetic material (ferrite) minimizes the leakage magnetic field. However, it can be confirmed that this does not apply to the dipole coil structure. Figure 11 shows a graphical representation of the magnetic field

strength simulation results, specifically for the yz-plane shown in Figure 9. As expected, in Figure 10, the dipole coil structure with the proposed reactive shield showed the lowest magnetic field intensity. In addition, it can be confirmed graphically that the magnetic field of comparison Case 2 is slightly lower than that of comparison Case 1, aligning with the results depicted in Figure 10.

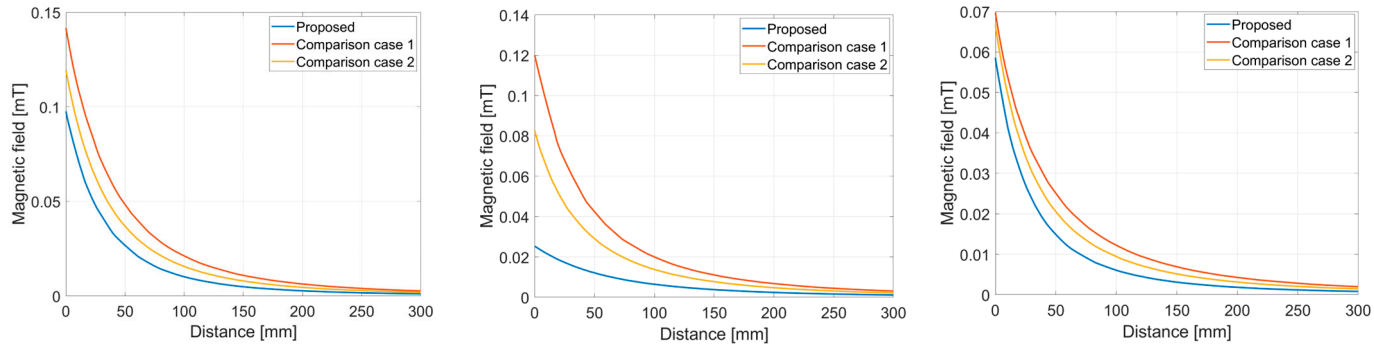

Figure 10. Magnetic field simulation results for each axis of the proposed reactive shield model and comparison groups: (**a**) *x*-axis, (**b**) *y*-axis, and (**c**) *z*-axis.

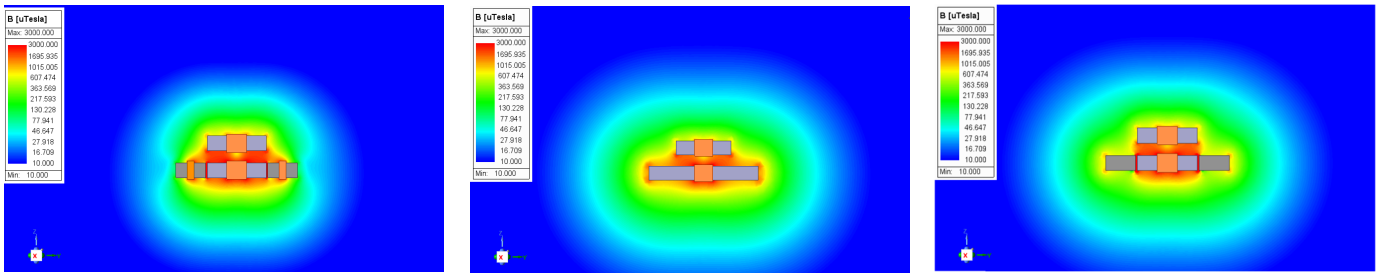

Figure 11. Graphical representation of magnetic field strength converted to the same magnetic field range: (**a**) proposed model, (**b**) comparison Case 1, and (**c**) comparison Case 2.

4. Validation of the Effectiveness of the Proposed Reactive Shield through Experiments

Figure 12 shows coil structures fabricated to experimentally validate the effectiveness of the proposed reactive shield for dipole coil structures. The geometric dimensions of the coil structures in Figure 12 align with the simulation setup shown in Figure 8 and Table 1. Dipole coils are fabricated using Litz wire with a diameter of 2.8 mm (0.05 mm/1300 strands) to reduce the AC resistance of the coils. In Figure 12, polycarbonate with a relative permeability of 1 is used as the gap between the TX, RX, and SH coils. In addition, the shape of the magnetic core is created by stacking several magnetic plates with a thickness of 5 mm and a relative magnetic permeability of 150. Table 5 shows the results of measuring the electrical parameters (inductance, equivalent series resistance) of the coils fabricated in Figure 12.

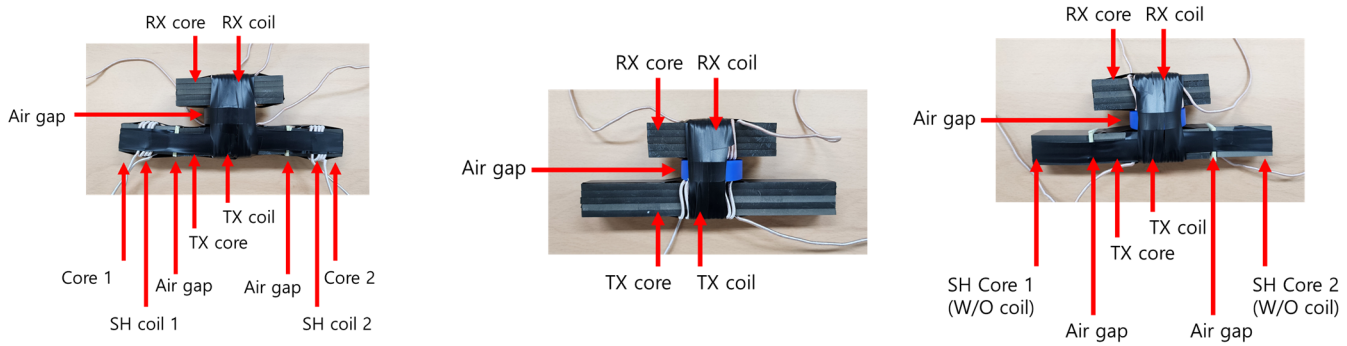

Figure 12. Dipole coil structures fabricated to validate the effectiveness of the reactive shield proposed through experiments: (**a**) proposed structure, (**b**) comparison Case 1—case with long TX ferrite, and (**c**) comparison Case 2—case in which only SH ferrite is added.

Table 5. Measured electrical parameters of fabricated coils.

Model	Parameters	Value
Proposed model	Inductance of TX coil (L_{TX})	30.0 μH
	Equivalent series resistance of TX coil (R_{TX})	30 mΩ
	Inductance of RX coil (L_{RX})	25.7 μH
	Equivalent series resistance of RX coil (R_{RX})	27 mΩ
	Mutual inductance between TX and RX ($M_{TX\text{-}RX}$)	6.01 μH
	Inductance of SH coils (L_{SH})	6.11 μH
	Equivalent series resistance of SH coils (R_{SH})	16 mΩ
	Mutual inductance between SH and TX ($M_{TX\text{-}SH}$)	3.78 μH
	Mutual inductance between SH and RX ($M_{RX\text{-}SH}$)	0.1 μH
Comparison Case 1	Inductance of TX coil (L_{TX})	34.2 μH
	Equivalent series resistance of TX coil (R_{TX})	37 mΩ
	Inductance of RX coil (L_{RX})	26.7 μH
	Equivalent series resistance of RX coil (R_{RX})	27 mΩ
	Mutual inductance between TX and RX ($M_{TX\text{-}RX}$)	6.15 μH
Comparison Case 2	Inductance of TX coil (L_{TX})	30.7 μH
	Equivalent series resistance of TX coil (R_{TX})	30 mΩ
	Inductance of RX coil (L_{RX})	26.7 μH
	Equivalent series resistance of RX coil (R_{RX})	27 mΩ
	Mutual inductance between TX and RX ($M_{TX\text{-}RX}$)	6.03 μH

Table 6 shows the resonant parameters of each circuit under 85 kHz resonant conditions. As can be seen from Table 5, the inductance of the TX and RX coils is different in each case. Therefore, to compensate circuit values for the changed coil inductances, the values of the compensation circuits must be different, which can be confirmed in Table 6. As explained previously, the LCC topology is applied to all TX sides, and the resonant conditions are as in (6). In all cases, the resonant value is calculated to ensure that the current of the TX coil is 6 A_{RMS}. As with the simulation, the V_{in} is selected as 60 V, and resonant parameters are calculated. Furthermore, a series topology is applied to the RX side with the same resonant conditions as (8). The resonant capacitance (C_{SH}) of the shield coil is 1410 nF, and the resonant frequency of the SH side is 54.2 kHz. Given that the system operating frequency (ω_o) is 85 kHz and the resonant frequency of the SH side (ω_{SH}) is 54.2 kHz, the SH side operates in the inductive region, as shown in Figure 5. As with the simulation, the notation of each circuit element aligns with Figure 4.

Table 6. Resonant circuit parameter values for the experiment.

Model	Parameters	Value
Proposed model	TX series inductance (L_{S1})	16.9 µH
	TX parallel capacitance (C_{P1})	203 nF
	TX series capacitance (C_{S1})	260 nF
	RX series capacitance (C_{S2})	136 nF
	SH capacitance (C_{SH})	1410 nF
Comparison Case 1	TX series inductance (L_{S1})	16.9 µH
	TX parallel capacitance (C_{P1})	203 nF
	TX series capacitance (C_{S1})	203 nF
	RX series capacitance (C_{S2})	136 nF
Comparison Case 2	TX series inductance (L_{S1})	17.0 µH
	TX parallel capacitance (C_{P1})	203 nF
	TX series capacitance (C_{S1})	256 nF
	RX series capacitance (C_{S2})	136 nF

Figure 13 shows the overall configuration for a WPT experiment. As shown in Figure 4, DC power is supplied from the DC power supply to the input and is subsequently delivered to the DC electronic load. The resonant elements on the TX, RX, and SH sides are configured, as shown in Figure 13. In addition, a full bridge inverter and rectifier are configured. All waveform measurements are performed using an oscilloscope, and DC input and output are referenced to the values displayed on the DC power supply and electronic load, respectively. Table 7 shows the measurement results of the WPT experiment. As in the previous simulation, the current of the TX coil ($\mathbf{I_{TX}}$) is fixed at 6 $A_{RMS,}$ and the power delivered to the load is fixed at 50 W. Similar to the simulation results, the output current in the proposed model is the highest when delivering 50 W to the load. Therefore, the power transfer efficiency in the proposed model is reduced by about 1.5% compared to comparison Case 1 and by about 0.3% compared to comparison Case 2. This is because, as shown from the measurement results in Table 5, the mutual inductance is the lowest in the WPT coils to which the proposed reactive shield is applied. Figure 14 shows the current waveforms of the TX and SH coils measured through an oscilloscope. As previously analyzed in Figures 6 and 7, the TX and SH coil currents are about 180° out of phase.

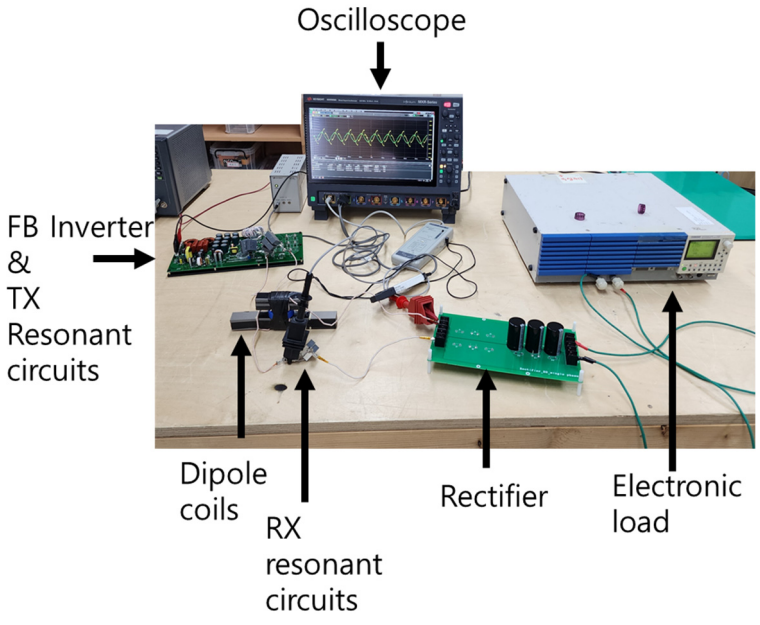

Figure 13. Setup for wireless power transfer experiments.

Table 7. Power transfer experiment results.

Model	Parameters	Value
Common condition	Operating frequency (ω_o)	85 kHz
	Target TX coil current (I_1)	6 A_{RMS}
	Target load power (P_{load})	50 W
Proposed model	Input voltage (V_{in})	60 V_{DC}
	Input current (I_{in})	1.15 A_{DC}
	Input power (P_{in})	69 W
	Output voltage (V_{load})	19.09 V_{DC}
	Output current (I_{load})	2.63 A_{DC}
	Output power (P_{out})	50.2
	Power transfer efficiency ($P_{out}/P_{in} \times 100$)	72.8%
Comparison Case 1	Input voltage (V_{in})	60 V_{DC}
	Input current (I_{in})	1.12 A_{DC}
	Input power (P_{in})	67 W
	Output voltage (V_{load})	20.6 V_{DC}
	Output current (I_{load})	2.43 A_{DC}
	Output power (P_{out})	50.1
	Power transfer efficiency ($P_{out}/P_{in} \times 100$)	74.2%
Comparison Case 2	Input voltage (V_{in})	60 V_{DC}
	Input current (I_{in})	1.15 A_{DC}
	Input power (P_{in})	69 W
	Output voltage (V_{load})	19.3 V_{DC}
	Output current (I_{load})	2.62 A_{DC}
	Output power (P_{out})	50.5
	Power transfer efficiency ($P_{out}/P_{in} \times 100$)	73.1%

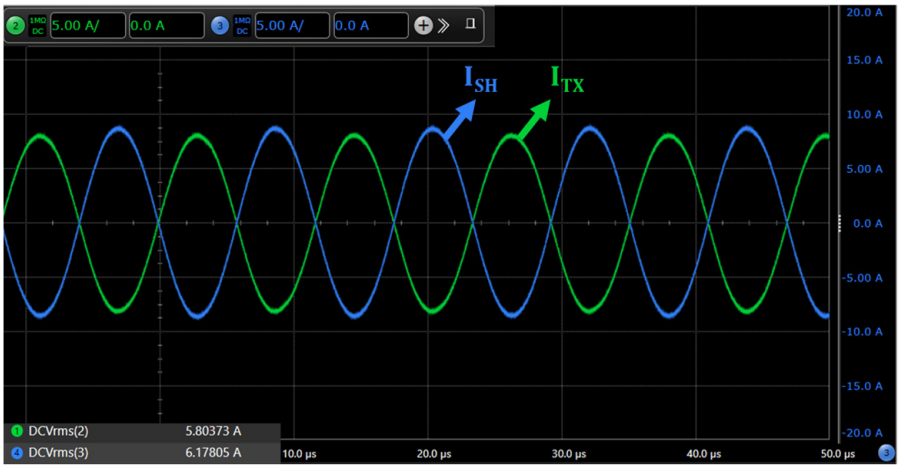

Figure 14. Measurement results of TX and SH coil currents in the proposed model.

Figure 15 shows how to measure the leakage magnetic field from each WPT coil. Magnetic field measurements are performed using NARDA's ELT-400 EMF antenna (measurement uncertainty of ELT-400: ±6%). Similar to the simulation, the measurement method involves varying the distance from the WPT coil in each axis direction, as shown in Figure 9. That is, the *x*-axis direction is measured in the horizontal direction of the coil, the *y*-axis direction is measured in the longitudinal direction of the coil, and the *z*-axis direction is measured in the height direction of the coil. The measured magnetic field is converted to Tesla (T) and recorded.

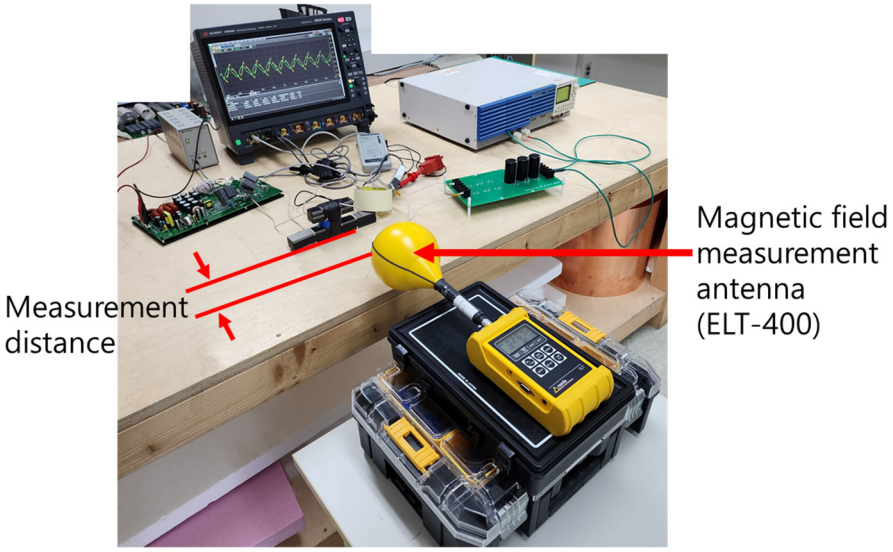

Figure 15. Measurement of the magnetic field from the WPT coil.

Figure 16 shows the measurement results of the magnetic field from each WPT coil. Similar to the previous simulation, the leakage magnetic field is the lowest in the dipole coil structure with the proposed reactive shield applied in all *x*-, *y*-, and *z*-axis directions. Specifically, the proposed model showed a magnetic field reduction rate ranging from 50.4% to 67.7% compared to comparison Case 1. Additionally, compared to comparison Case 1, the magnetic field reduction rate is shown to be from a minimum of 17.4% to a maximum of 41.8%. The decrease is particularly high in the longitudinal direction (*y*-axis) of the magnetic core.

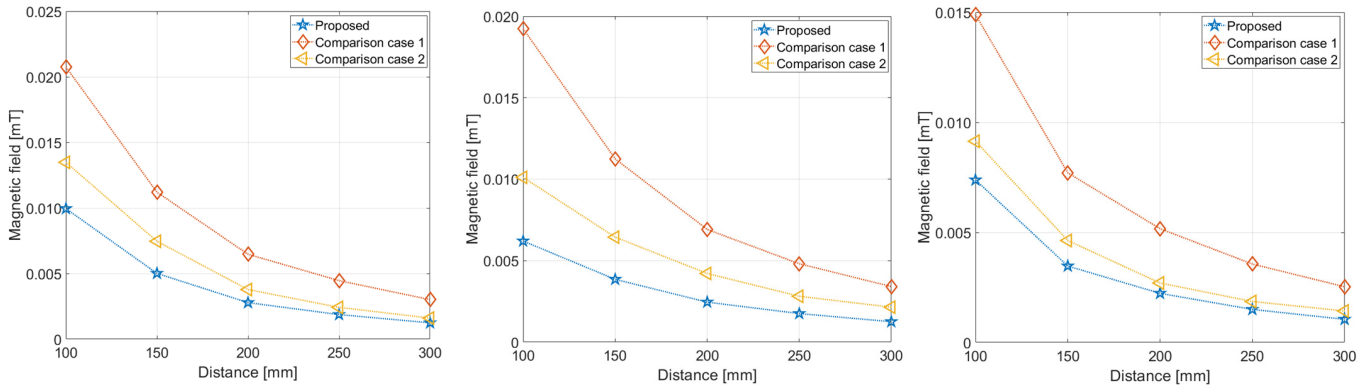

Figure 16. Magnetic field measurement results depending on the distance from the WPT coil system: (**a**) *x*-axis, (**b**) *y*-axis, and (**c**) *z*-axis.

Finally, Figure 17 shows the measured magnetic field (measured at 300 mm in the *y*-axis direction) and power transfer efficiency of the dipole coil with the proposed reactive shield and the comparison case. Compared to the comparison groups, the proposed reactive shield reduces power transfer efficiency by about 1.5% and 0.3%, respectively. This can be attributed to the cancellation of some of the magnetic fields generated from the TX coil with the SH coil, as shown in Figure 7, resulting in a decrease in mutual inductance and, thus, a decrease in efficiency. However, the leakage magnetic field, a significant problem in the dipole structure, is reduced by up to 63% compared to the comparison groups. This illustrates a trade-off relationship between efficiency and the magnetic field. However, in applications in which leakage magnetic fields are a crucial design indicator, the dipole structure for the reactive shield is deemed sufficiently useful.

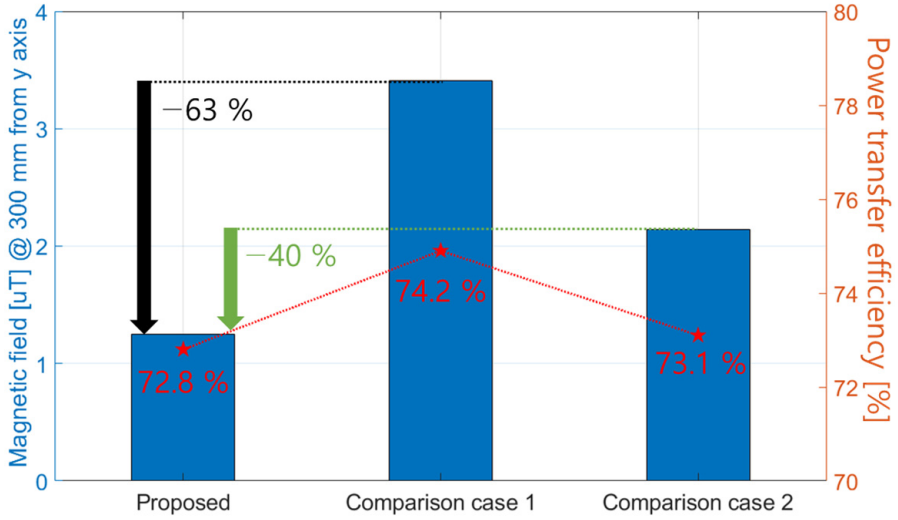

Figure 17. Comparison of the magnetic field and power transfer efficiency of the proposed model and comparison groups.

5. Conclusions

This paper proposes a reactive shield for a WPT system using dipole coils. The dipole coil structure has a magnetic field that radiates in the length direction of the magnetic core, making leakage magnetic fields a significant design concern. The reactive shield for the dipole structure proposed in this paper is designed to resonate at a frequency lower than that of the operating frequency and operates in an inductive region where the reactance is positive. Therefore, the magnetic field induced by the current in the reactive shield is generated in the direction opposite to the magnetic field of the TX coil, thereby reducing the leakage magnetic field. The method for designing the shield coil was mathematically analyzed, and the current and magnetic field phases of each coil were compared. In addition, through simulation and experiment, the effectiveness of the reactive shield was validated in a 50 W class WPT system. Specifically, it was experimentally validated that in a WPT system with a reactive shield, the power transfer efficiency is reduced by at least 0.3% to up to 1.5%, whereas the leakage magnetic field is reduced by up to 68%. Although the shielding system increases the weight, size, and cost of the TX side, the 68% reduction in leakage magnetic fields is well worth it. Since there is no need to include a separate SH system on the RX side, the proposed system is judged to be sufficiently valuable. Therefore, the reactive shield proposed in this paper is sufficiently effective in a WPT system adopting dipole-type coils, where the leakage magnetic field is a crucial design factor. In particular, it is expected that the magnetic field shielding method proposed in this paper can be actively used in human body implantable applications where reducing leakage magnetic fields is very important.

Author Contributions: Conceptualization, investigation, writing—review and editing and methodology, Y.S.; validation, investigation, supervision, and visualization, S.W. All authors have read and agreed to the published version of the manuscript.

Funding: This work was supported by the Institute of Information & communications Technology Planning & Evaluation (IITP) grant funded by the Korea government (MSIT) (No. 2020-0-00839, Development of Advanced Power and Signal EMC Technologies for Hyper-connected E-Vehicle).

Data Availability Statement: The data presented in this study are available on request from the corresponding authors.

Acknowledgments: We would like to acknowledge the technical support from Ansys Korea.

Conflicts of Interest: The authors declare no conflicts of interest.

Appendix A

In Appendix A, two of the contents of the text are verified through simulation. The first is whether it is reasonable to consider only two inductances out of six mutual inductances in Figure 4 of the text, and the second is whether the approximation of inductance calculations as in (4) and (5) is reasonable. Table A1 shows the inductance extraction values for the model that separates the windings of the two SH coils in Figure 8a and the model that combines the windings.

Table A1. Electrical parameters of the coil measured according to winding connection and disconnection.

Model	Parameters	Value (μH)
Model with SH coil windings combined (Figure 4a)	Inductance of TX coil (L_{TX})	29.51
	Inductance of RX coil (L_{RX})	25.4
	Mutual inductance between TX and RX ($M_{TX\text{-}RX}$)	6.2
	Inductance of SH coil 1 (L_{SH1})	2.75
	Inductance of SH coil 2 (L_{SH2})	2.75
	Mutual inductance between TX and SH1 ($M_{TX\text{-}SH1}$)	1.95
	Mutual inductance between TX and SH2 ($M_{RX\text{-}SH2}$)	1.96
	Mutual inductance between RX and SH1 ($M_{RX\text{-}SH1}$)	0.0036
	Mutual inductance between RX and SH2 ($M_{RX\text{-}SH2}$)	0.0035
	Mutual inductance between SH1 and SH2 ($M_{SH1\text{-}SH2}$)	0.0157
Model with separated SH coil windings (Figure 4b)	Inductance of TX coil (L_{TX})	29.51
	Inductance of RX coil (L_{RX})	25.4
	Mutual inductance between TX and RX ($M_{TX\text{-}RX}$)	6.2
	Inductance of SH coil 2 (L_{SH2})	5.82
	Mutual inductance between TX and SH ($M_{TX\text{-}SH}$)	3.91
	Mutual inductance between RX and SH ($M_{RX\text{-}SH}$)	0.0071

First, both simulation results show that the mutual inductance between the RX and SH shields ($M_{RX\text{-}SH1}$, $M_{RX\text{-}SH2}$, and $M_{RX\text{-}SH}$) is minimal. Therefore, it is logically reasonable not to consider this. Next, to verify (4) in the text, if we substitute the self-inductances of the SH coils (L_{SH1} and L_{SH2}) with separated windings and the mutual inductance between the SH coils ($M_{SH1\text{-}SH2}$) into (4), it is exactly the same as the self-inductance value of the SH coil with the windings combined (L_{SH}). However, given the minimal mutual inductance between SH coils ($M_{SH1\text{-}SH2}$), the approximation used in (4) is valid. Finally, considering the mutual inductance between the TX and the SH coils, we can see that the sum of the mutual inductances of the SH coil's windings separated ($M_{TX\text{-}SH1}$ and $M_{TX\text{-}SH2}$) is exactly the same as that of the mutual inductance of the windings combined as one ($M_{TX\text{-}SH}$), as shown in Equation (5). Therefore, (5) can also be found to be valid.

Appendix B

In Appendix B, power transfer efficiency and shielding performance are analyzed according to changes in the resonant frequency of the SH coil and changes in the number of turns of the SH coil.

First, to change the resonant frequency of the SH coil, a parameter sweep is conducted on the SH side resonant capacitance (C_{SH}) from 1000 nF to 4000 nF in 500 nF increments. If C_{SH} changes while SH coil inductance L_{SH} is constant, the resonant frequency changes, and both system efficiency and shielding performance change. Table A2 shows the SH side

resonant frequency and SH coil current according to changes in SH capacitance C_{SH}. As can be seen from (10) to (13), the lower the resonant frequency on the SH side, the larger the impedance Z_{SH} on the SH side, so Table A2 shows that the SH current decreases.

Additionally, Figure A1 shows the WPT power transfer efficiency and leakage magnetic field according to the resonant capacitance (resonant frequency) of the SH side. In Table A2, when the SH coil resonant frequency is large, the SH coil current increases, which means that the loss due to the SH coil increases, so the power transfer efficiency increases. On the other hand, as the SH coil current increases, the leakage magnetic field also decreases because the shielding magnetic field generated by the SH coil increases. Conversely, when the SH coil resonant frequency decreases and the SH coil current decreases, efficiency increases, but shielding performance decreases. In other words, it is confirmed that efficiency and power transfer efficiency have a trade-off relationship.

Table A2. Changes in SH side resonant frequency and SH coil current depending on SH side capacitance C_{SH} change.

SH Capacitance (C_{SH}) [nF]	**1000**	**1500**	**2000**	**2500**	**3000**	**3500**	**4000**
Resonant frequency [kHz]	64	53	46	41	37	34	32
SH coil current [A_{RMS}]	9.15	6.01	5.13	4.72	4.47	4.32	4.2

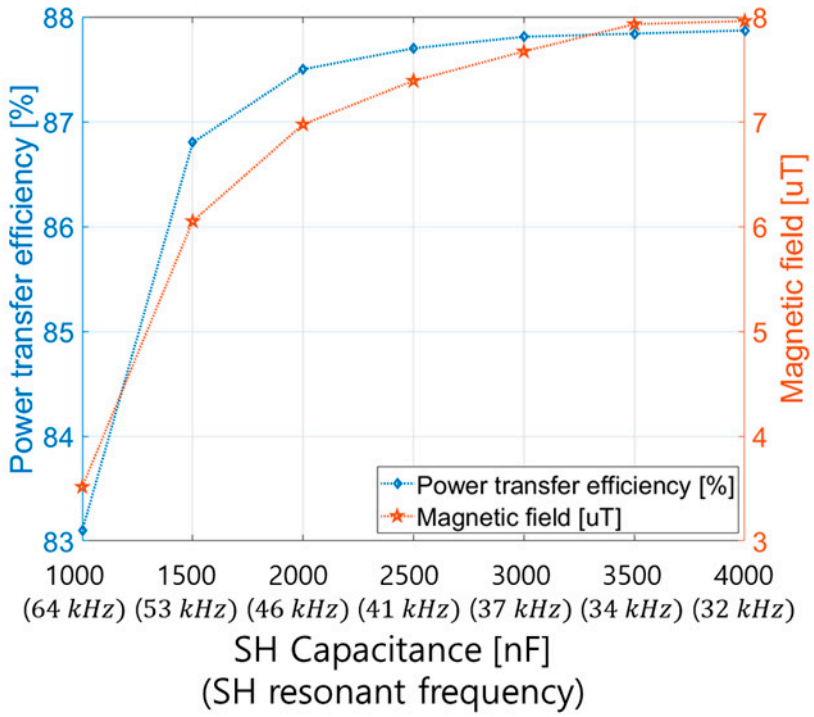

Figure A1. Changes in power transfer efficiency and leakage magnetic field according to changes in SH side capacitance.

Table A3. Changes in SH side inductance and SH coil current according to SH coil turns change.

SH Coil Turns [Turns]	**2**	**3**	**4**	**5**	**6**	**7**	**8**
L_{SH} [μH]	1.46	3.29	5.84	9.13	1.31	1.79	2.34
$M_{TX\text{-}SH}$ [μH]	1.97	2.95	3.93	4.92	5.94	6.87	7.86
SH coil current [A_{RMS}]	12.8	8.54	64.1	5.15	4.35	3.67	3.22

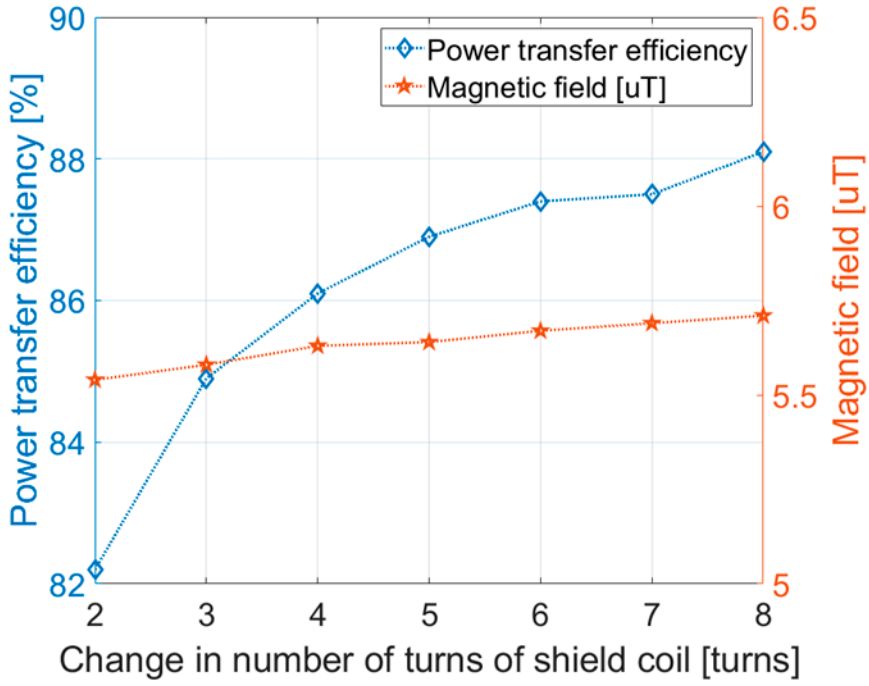

Figure A2. Changes in power transfer efficiency and leakage magnetic field according to changes in SH coil turns.

In another parameter sweep, the power transfer efficiency and shielding performance at different turns of the SH coil are analyzed. Figure A2 shows the change in SH side inductance (L_{SH}, $M_{TX\text{-}SH}$) and SH coil current according to the number of SH coil turns. As the number of SH coil turns increases, the inductances increase, but since the capacitance (C_{SH}) on the SH coil side remains the same, the SH coil current decreases. And Figure A2 shows the power transfer efficiency and leakage magnetic field according to the number of SH coil turns. As the number of SH turns increases, the current decreases and the efficiency increases rapidly, but the shielding performance also slowly decreases. In other words, the shielding performance is maintained to some extent. This is because the number of turns of the SH coil increases, and the magnetomotive force is maintained.

Appendix C

In Appendix C, an analysis is conducted on changes in design parameters due to the magnetic core. Figure A3 shows a typical dipole coil structure represented as a magnetic circuit. $R_{1\text{-}1}$, $R_{1\text{-}2}$, $R_{2\text{-}1}$, and $R_{2\text{-}2}$ represent the magnetic reluctance of the TX and RX coils and magnetic core, respectively, and $R_{12\text{-}1}$ and $R_{12\text{-}2}$ represent the reluctance of the air gap between TX and RX. If $R_{1\text{-}1}$, $R_{1\text{-}2}$, $R_{2\text{-}1}$, and $R_{2\text{-}2}$ are expressed as R_{core} and $R_{12\text{-}1}$ and $R_{12\text{-}2}$ are expressed as R_{air}, reluctance can be expressed as (A1), (A2):

$$R_{core} = \frac{l_{core}}{\mu_{core} A_{core}} \tag{A1}$$

$$R_{air} = \frac{l_{air}}{\mu_{air} A_{air}} \tag{A2}$$

In (A1) and (A2), l and A represent the length and cross-sectional area, respectively, and μ_{core} and μ_{air} represent the permeability of the core and air, respectively. In general, μ_{core} is a hundred to several thousand times larger than μ_{air}. Therefore, R_{core} and R_{air} have the same relationship as (A3):

$$R_{air} \gg R_{core} \tag{A3}$$

Therefore, what can be inferred from (A3) is that it is the air gap, not the permeability or shape of the magnetic material, that determines the magnetic flux of the WPT system.

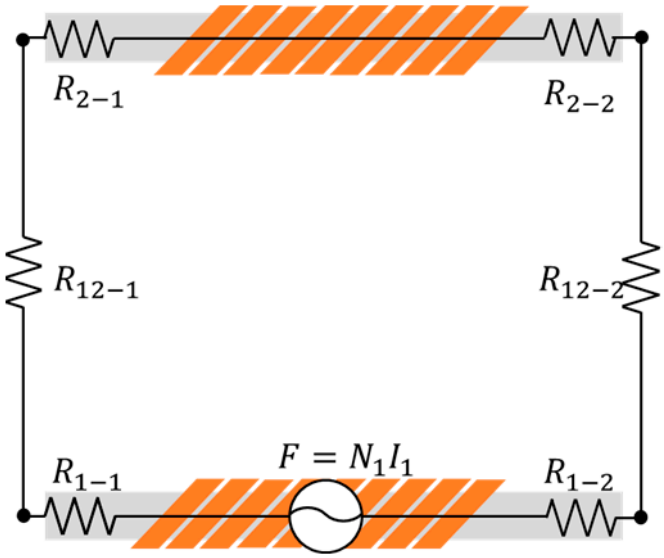

Figure A3. A typical dipole coil structure modeled as a magnetic circuit.

Table A4. Change in circuit parameter values according to change in permeability of magnetic core in dipole coil structure.

Permeability of Core	L_{TX} (μH)	L_{RX} (μH)	$M_{TX\text{-}RX}$ (μH)	L_{SH} (μH)	$M_{TX\text{-}SH}$ (μH)
150	29.52	25.41	6.2	5.82	3.91
650	30.06	25.75	6.32	5.93	4.04
1150	30.46	26.03	6.47	5.96	4.14
1650	30.60	26.12	6.54	5.99	4.17
2150	30.71	26.21	6.57	6.00	4.19

Table A4 shows the results of extracting the electrical parameters by simulating changes in the magnetic permeability of the magnetic cores in the proposed model of Figure 8a. Although the permeability of the core varied in the range of up to 2000 (up to 1300%), the inductance changes of the coils are only up to 7%. In other words, it can be concluded that in a WPT system adopting a reactive shield, the permeability of the core or core is not that important. This is because, as can be seen from (A1) to (A3), the magnetic permeability of the core is much larger than that of air, and the magnetic reluctance due to the air gap is very dominant in the WPT system with a dipole structure. However, on the other hand, this means that the structure of the core that determines the voids will be very important.

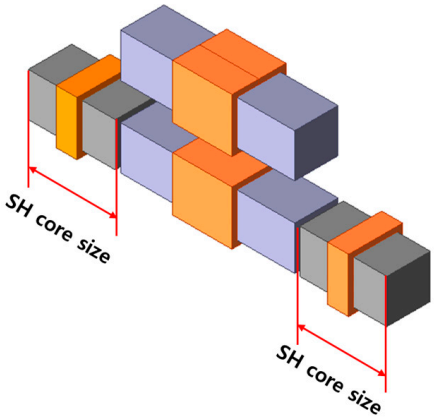

Figure A4. Simulation setup according to SH core shape and size.

Table A5. Change in circuit parameter values according to change in SH core shape and structure in dipole coil structure.

SH Core Size [mm]	40	42	44	46	48	50	52
$M_{TX\text{-}SH}$ [μH]	2.39	2.61	2.85	3.13	3.48	3.94	4.57
SH coil current [A_{RMS}]	4.7	4.95	5.21	5.5	5.87	6.33	6.94

Next, to check various performance changes of the WPT system with a dipole coil structure according to the structure of the SH core, simulations are performed as shown in Figure A4. Simulations are performed by varying the size of the SH core in the longitudinal direction. Note that, except for the structure of the SH core, the number of turns of the SH coil, and all parameters on the TX and RX sides are kept the same. Table A5 shows the change in current of mutual inductance between TX and RX ($M_{TX\text{-}SH}$) and SH coil according to the size of the SH core. Table A5 shows that the larger the SH core size, the larger the $M_{TX\text{-}SH}$, and thus the increased current induced in the SH coil. This is because the larger the SH core, the larger the voltage induced in the SH coil and the larger the current.

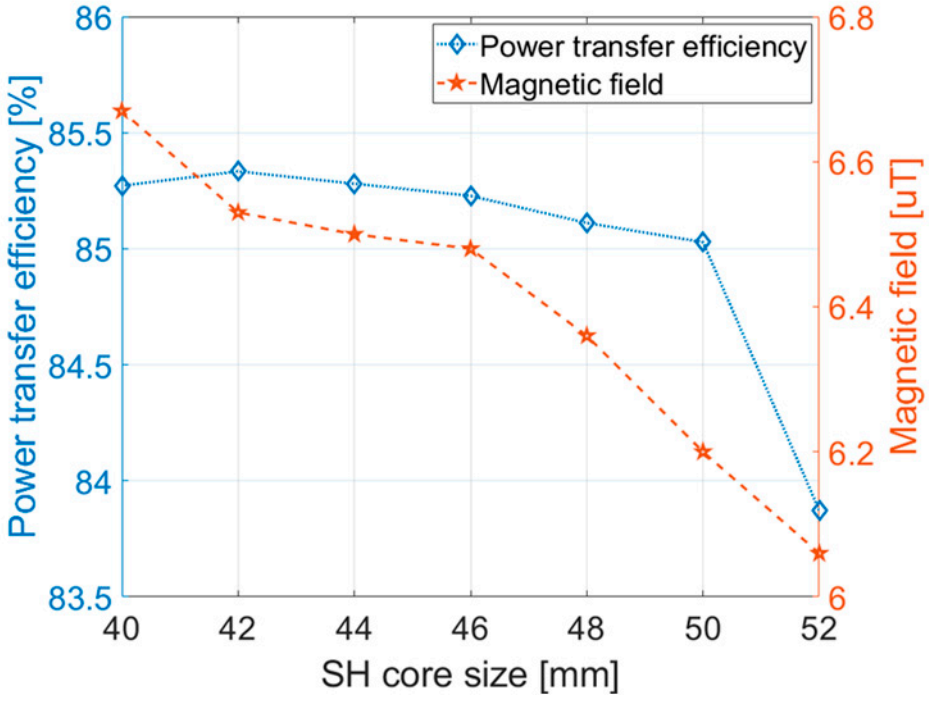

Figure A5. Changes in power transfer efficiency and leakage magnetic field according to changes in SH core size.

Figure A5 shows the results of simulating changes in power transfer efficiency and leakage magnetic field according to core size. The leakage magnetic field is simulated at 100 mm in the y-direction of the coil. As the core size increases, the SH coil current increases, which improves SH performance and reduces the leakage magnetic field, but on the other hand, the power loss increases due to the current flowing in the SH coil. Therefore, it can be concluded that, unlike the permeability of the previous core, the structure of the SH core is a very important factor in determining SH performance.

References

1. Abou Houran, M.; Yang, X.; Chen, W. Magnetically coupled resonance WPT: Review of compensation topologies, resonator structures with misalignment, and EMI diagnostics. *Electronics* **2018**, *7*, 296. [CrossRef]
2. Arif, S.M.; Lie, T.T.; Seet, B.C.; Ayyadi, S.; Jensen, K. Review of electric vehicle technologies, charging methods, standards and optimization techniques. *Electronics* **2021**, *10*, 1910. [CrossRef]

3. Nguyen, M.T.; Nguyen, C.V.; Truong, L.H.; Le, A.M.; Quyen, T.V.; Masaracchia, A.; Teague, K.A. Electromagnetic field based WPT technologies for UAVs: A comprehensive survey. *Electronics* **2020**, *9*, 461. [CrossRef]
4. Rayan, B.A.; Subramaniam, U.; Balamurugan, S. Wireless Power Transfer in Electric Vehicles: A Review on Compensation Topologies, Coil Structures, and Safety Aspects. *Energies* **2023**, *16*, 3084. [CrossRef]
5. Van Mulders, J.; Delabie, D.; Lecluyse, C.; Buyle, C.; Callebaut, G.; Van der Perre, L.; De Strycker, L. Wireless Power Transfer: Systems, Circuits, Standards, and Use Cases. *Sensors* **2022**, *22*, 5573. [CrossRef] [PubMed]
6. Okasili, I.; Elkhateb, A.; Littler, T. A review of wireless power transfer systems for electric vehicle battery charging with a focus on inductive coupling. *Electronics* **2022**, *11*, 1355. [CrossRef]
7. Shin, Y.; Hwang, K.; Park, J.; Kim, D.; Ahn, S. Precise vehicle location detection method using a Wireless Power Transfer (WPT) system. *IEEE Trans. Veh. Technol.* **2019**, *68*, 1167–1177. [CrossRef]
8. Manko, R.; Vukotić, M.; Makuc, D.; Vončina, D.; Miljavec, D.; Čorović, S. Modelling of the Electrically Excited Synchronous Machine with the Rotary Transformer Design Influence. *Energies* **2022**, *15*, 2832. [CrossRef]
9. Kim, D.; Park, J.; Park, B.; Shin, Y.; Kim, K.; Park, H.; Ahn, S. Propulsion and rotation of microrobot based on a force on a magnetic material in a time-varying magnetic field using a wireless power transfer system. *IEEE Trans. Magn.* **2019**, *56*, 6700105. [CrossRef]
10. Prosen, N.; Domajnko, J. Optimization of a circular planar spiral wireless power transfer coil using a genetic algorithm. *Electronics* **2024**, *13*, 978. [CrossRef]
11. Domajnko, J.; Prosen, N. A z-axis-tolerant inductive power transfer system using a bipolar double D receiver coil structure. *Electronics* **2023**, *12*, 4303. [CrossRef]
12. Shin, Y.; Woo, S.; Rhee, J.; Lee, C.; Kim, H.; Huh, S.; Park, B.; Ahn, S. Accurate method for extracting the coupling coefficient of an LCC-series wireless power transfer system. *IEEE Trans. Power Electron.* **2022**, *37*, 11406–11422. [CrossRef]
13. Kuglics, L.; Géczy, A.; Dusek, K.; Busek, D.; Illés, B. Personal Air-Quality Monitoring with Sensor-Based Wireless Internet-of-Things Electronics Embedded in Protective Face Masks. *Sensors* **2024**, *24*, 2601. [CrossRef] [PubMed]
14. Sari, V. Design and Implementation of a Wireless Power Transfer System for Electric Vehicles. *World Electr. Veh. J.* **2024**, *15*, 110. [CrossRef]
15. Huh, H.; Bui, G.; Seo, C. Efficient compact radiative near-field wireless power transfer to miniature biomedical implants. *IEEE Antennas Wirel. Propag. Lett.* **2023**, *22*, 2803–2807.
16. Cha, H.; Park, W.; Je, M. A CMOS rectifier with a cross-coupled latched comparator for wireless power transfer in biomedical applications. *IEEE Trans. Circuits Syst. II* **2012**, *59*, 409–413. [CrossRef]
17. Das, M.; Jeong, S.; Sim, B.; Lee, S.; Hong, S.; Kim, Y.; Kim, J. Series Topology for Suppressing Electromagnetic Interference (EMI) for Digital TV Wireless Power Transfer (WPT) Systems Study of Series. In Proceedings of the IEEE Electrical Design of Advanced Packaging and Systems Symposium (EDAPS), Chandigarh, India, 16–18 December 2018; Volume 2019.
18. ICNIRP. *Guidelines for limiting exposure to time-varying electric, magnetic, and electromagnetic fields (up to 300 GHz) Heath Phys.* **1998**, *74*, 494–521.
19. *IEC PAS 63184*; Assessment Methods of the Human Exposure to Electric and Magnetic Fields from Wireless Power Transfer Systems–Models, Instrumentation, Measurement and Numerical Methods and Procedures (Frequency Range of 1 kHz to 30 MHz). IEC: Geneva, Switzerland, 2021.
20. Choi, B.; Thai, V.; Lee, E.; Kim, J.; Rim, C. Dipole-coil-based wide-range inductive power transfer systems for wireless sensors. *IEEE Trans. Ind. Electron.* **2016**, *63*, 3158–3167. [CrossRef]
21. Park, C.; Lee, S.; Cho, G.; Rim, C. Innovative 5-m-off-distance inductive power transfer systems with optimally shaped dipole coils. *IEEE Trans. Power Electron.* **2014**, *30*, 817–827. [CrossRef]
22. Rong, C.; He, X.; Zeng, Y.; Lu, C.; Liu, M.; Orientation, H.-E. High-Efficiency Orientation Insensitive WPT systems using magnetic dipole coil for low-power devices. *IEEE Trans. Power Electron.* **2022**, *37*, 4985–4990. [CrossRef]
23. Rong, C.; He, X.; Liu, M.; Wang, Y.; Liu, X.; Lu, C.; Zeng, Y.; Liu, R. Omnidirectional free-degree wireless power transfer system based on magnetic dipole coils for multiple receivers. *IEEE Access* **2021**, *9*, 81588–81600. [CrossRef]
24. Khan, S.R.; Pavuluri, S.K.; Cummins, G.; Desmulliez, M.P.Y. Wireless power transfer techniques for implantable medical devices: A review. *Sensors* **2020**, *20*, 3487. [CrossRef] [PubMed]
25. Park, J.; Kim, D.; Hwang, K.; Park, H.; Kwak, S.; Kwon, J.; Ahn, S. A resonant reactive shielding for planar wireless power transfer system in smartphone application. *IEEE Trans. Electromagn. Compat.* **2017**, *59*, 695–703. [CrossRef]
26. Lee, C.; Woo, S.; Shin, Y.; Rhee, J.; Moon, J.S. EMI Reduction Method for Wireless Power Transfer Systems With High Power Transfer Efficiency Using Frequency Split Phenomena. *IEEE Trans. Electromagn. Compat.* **2022**, *64*, 1683–1693. [CrossRef]
27. Kim, J.; Ahn, S. Dual loop reactive shield application of wireless power transfer system for leakage magnetic field reduction and efficiency enhancement. *IEEE Access* **2021**, *9*, 118307–118323. [CrossRef]
28. Wei, Y.; Wu, F. Indirect control strategy of secondary current for LCC-series compensated wireless power transfer system based on primary current closed-loop control. *IEEE Trans. Transp. Electrif.* **2022**, *8*, 1553–1565. [CrossRef]
29. ElGhanam, E.; Hassan, M.; Osman, A. Design of a High Power, LCC-Compensated, Dynamic, Wireless Electric Vehicle Charging System with Improved Misalignment Tolerance. *Energies* **2021**, *14*, 885. [CrossRef]

30. Yenil, V.; Cetin, S. An Improved Pulse Density Modulation Control for Secondary Side Controlled Wireless Power Transfer System Using LCC-S Compensation. *IEEE Industrial Electron.* **2022**, *69*, 12762–12772. [CrossRef]
31. Chen, C.-L.; Hung, C.-W. Improving LCC Series-Based Wireless Power Transfer System Output Power at High Temperature. *Electronics* **2021**, *10*, 2875. [CrossRef]